Extreme Mechanics Letters 41 (2020) 101042

Contents lists available at ScienceDirect

Extreme Mechanics Letters

journal homepage: www.elsevier.com/locate/eml

Is the Bouligand architecture tougher than regular cross-ply laminates? A discrete element method study

J. William Pro [b], Francois Barthelat [a,b,*]

[a] Department of Mechanical Engineering, University of Colorado, 427 UCB, 1111 Engineering Dr, Boulder, CO 80309, United States
[b] Department of Mechanical Engineering, McGill University, 817 Sherbrooke Street West, Montreal, QC H3A 2K6, Canada

ARTICLE INFO

Article history:
Received 21 May 2020
Received in revised form 26 August 2020
Accepted 26 September 2020
Available online 16 October 2020

Keywords:
Discrete element modeling
Bouligand structures
Fracture mechanics
Cross-ply
Crack resistance
Toughness

ABSTRACT

The Bouligand structure, prominent in arthropod cuticles and fish scales, is a fibrous laminate where the orientation of the fibers increases incrementally across the thickness. Complex three-dimensional fracture mechanisms (crack twisting) have recently been intriguing researchers as a potential source of toughness. Capturing the interaction of propagating cracks with this complex architecture, however, remains a challenge and usually requires computationally expensive models. We ask the question: Given identical fibers and interfaces, is the Bouligand architecture tougher than other types of cross-plies? Here we use the discrete element method (DEM) to capture the main fracture mechanisms in fibrous laminates: crack deflection, crack twisting, delamination, process zone and fiber fracture, and to capture how various contrasts of properties between fibers and matrix affect these mechanisms. Our main conclusion is that in terms of fracture toughness (initiation and propagation), the Bouligand is outperformed by the (0°/90°) cross-ply for any crack orientation. The Bouligand structure is however more isotropic in-plane in terms of both stiffness and toughness, which may confer some advantage for multiaxial loading and could explain why this architecture is often found in nature.

1. Introduction

Fibrous lamellar structures are ubiquitous in biological materials [1] and consist of fibers ordered in unidirectional 'plies', which confer these materials with high stiffness and exceptionally high fracture toughness [2–5]. Crossply structures (0°/90°) are found in plant and wood [6], lamellar bone [7], conch shell [8], fish scales [9], and rodent enamel [10–13]. In the Bouligand structure the orientation of the fibers increases incrementally across the thickness, forming a helical 3D structure. The Bouligand structure is found in arthropod cuticles [14,15] including crab exoskeleton, lobster claws, beetle shells, mantis shrimp [16–18], as well as in certain fish scales including *Arapaima gigas*, Coelacanth, and the Australian lung fish [19]. Interestingly, some fish scales exhibit characteristics of both a Bouligand and a crossply architecture, most notably the Arapaima gigas; therefore fish scales fall in both categories [19–21]. While many experimental investigations of the mechanics of crossply and Bouligand structures were reported [10–12,17,18,22–26], numerical and analytical models of crack propagation are lacking substantially. Theoretical fracture mechanics has been used to capture the effect of the helicoidal architecture on the crack driving force in Bouligand structures [27,28], but these models are bound by LEFM limitations and do not predict fracture toughness/resistance. Intrinsic cohesive zone models (CZM) have been proposed for Bouligand structures [23] to capture crack twisting. However these models are limited to pre-defined crack paths that ignore the fracture of individual fibers, and post-initiation crack resistance (*R*-curve) data was not reported. Recent phase field models considered crack propagation in single and double twisted Bouligand architectures, but only reported the initiation fracture toughness and did not study in-depth the effects of the relative pitch angle between the plies [19]. Capturing crack propagation in the Bouligand architecture is challenging and computationally expensive because the architecture, crack propagation and micro-mechanisms are fully three-dimensional and cannot be reduced to two dimensional problems. The problem is further complicated by multiple possible failure modes (interface delamination, fiber pullout, fiber fracture), multiple toughening mechanisms occurring simultaneously (crack deflection, twisting, bridging), and large inelastic process zones developing near the crack tip, requiring non-linear approaches to fracture mechanics. Computational costs are often prohibitive using standard methods such as finite elements. Recently we have used the discrete element method (DEM) to capture interacting failure mechanisms (simultaneous rod and interface fracture), crack propagation, and toughening mechanisms in tooth enamel, a complex 3D biocomposite [29,30]. These models were inspired from the micro-architecture found in human

* Corresponding author at: Department of Mechanical Engineering, University of Colorado, 427 UCB, 1111 Engineering Dr, Boulder, CO 80309, United States.
E-mail address: francois.barthelat@colorado.edu (F. Barthelat).

https://doi.org/10.1016/j.eml.2020.101042
2352-4316/

enamel and many other species, where the rods form a criss-crossing pattern (or 'decussating') that resembles a crossply at a local level; this feature has been reproduced by biological growth models and is known to enhance fracture toughness [13,31]. In this report we use our DEM based fracture mechanics models to capture crack propagation in fibrous lamellar structures, including the Bouligand architecture and (0°/90°) cross plies.

2. Material model & fracture simulation setup

The fibrous composite architectures and their corresponding DEM models are shown on Fig. 1. To simplify the computation and to ensure space filling we assumed fibers with a square cross section $w \times w$. While the cross sections in most biological materials are generally more complex and non-square, more recent synthetic systems use fibers with cross-sections that are nearly square and therefore we would expect our models to represent these systems more closely [25]. In general the DEM approach is robust and can model other types of fiber cross sections, but this simple representation captures the main effects of the twisting lamellar architecture. The fibers are arranged in plies, each consisting of one layer of uniformly spaced parallel fibers. Different types of fibrous lamellar structures were created from this basic building block. As a reference fibrous architecture we considered the classical crossply, denoted C(0°/90°) , where fiber orientation alternates between 0° and 90° (Fig. 1a). In the Bouligand architecture the angle of the fiber increases from one ply to the next incrementally and by a relative ply angle $\gamma \leq$ 90°, with the first ply oriented at $+\frac{1}{2}\gamma$ so that the horizontal symmetry plane bisects two adjacent plies at $+\frac{1}{2}\gamma$ and $\frac{1}{2}\gamma$; here the Bouligand structure is denoted as B(γ) (Fig. 1b). The C(0°/90°) crossply and B(γ) Bouligand can therefore be differentiated by the absolute angle between the plies and by the stacking sequence: In the C(0°/90°) crossply the sequence of angles alternates between 0° and 90°, while in the B(γ) Bouligand the angle increases incrementally by the relative ply angle γ. To delineate the effect of stacking sequence and fiber angles we consider a third crossply architecture, where the ply angle alternates between $+\frac{1}{2}\gamma$ and $-\frac{1}{2}\gamma$ (Fig. 1c), denoted as C($+\frac{1}{2}\gamma$ /$-\frac{1}{2}\gamma$). Using this formulation, the B(γ) Bouligand and C($+\frac{1}{2}\gamma/-\frac{1}{2}\gamma$) are identical when γ=90°, and are equivalent to a 45° rotation of the C(0°/90°) crossply about the z-axis. Note that by using this model of the ply configuration, we restrict our attention to fibrous systems where the relative ply angle is constant in magnitude (but may alternate in sign). Indeed in some biological systems, in particular the Arapaima gigas [19], the ply orientation follows a "double Bouligand" structure with ply layup $\gamma i/(\gamma+\pi/2)\ i/\gamma(i+1)/\ (\gamma+\pi/2)(i+1)\ldots/\gamma n/(\gamma+\pi/2)(n)$, where i is the layer index and n is the total number of layers.

We built DEM models of these architectures by first seeding the fibers with nodes of uniform spacing l_e along their centerlines. We use the nodes to mesh individual fibers with standard 3D Bernoulli–Euler beam elements (modulus E_f and density ρ_f) that captured bending, axial, and torsional deformation of the individual fibers (Fig. 1d). The fibers were assumed to completely fracture when the maximum tensile stress in the fiber exceeded the ultimate fiber strength σ_f. This is a stress-based failure criterion that assumes the fiber constituents are perfectly brittle, which is reasonable for highly mineralized (95%–99%) hard biological composite systems (e.g., enamel, etc.) [32]. We also idealized the fiber strengths to be completely uniform with no statistical distribution; future DEM models could implement Weibull-type failure statistics in the fibers as in our previous DEM models [30,33,34]. Multi-axial interface cohesive elements were inserted between the fibers within a single ply (intra-ply) orthogonal to the fiber elements and also between all fibers in two adjacent plies (inter-ply). The force generated by the individual cohesive elements was function of cohesive law (described below) and of the overlap area between the neighboring fibers. The effective area of the intra-ply elements was simply $A_i = w \times l_e$ where w is the width of the fibers and l_e is the length of the element. The inter-ply elements had a more complex parallelogram geometry (Fig. 1e), with an effective area given by $A_i = w^2/sin(\gamma)$ for γ > 0°and $A_i = w \times l_e$ for the special case where the fibers are all aligned (γ = 0°). Note that this interface representation assumes nearest neighbor connectivity between crossing fibers in adjacent plies, which is only valid when the fiber volume fraction $\phi_f = w/(2t_i+w)$ is large, where t_i is the interface thickness; this requirement for ϕ_f presents a central limitation of the DEM model applicability. The cohesive law used for both interply and intraply interfaces (Fig. 1f) was defined by four independent parameters: the interface stiffness k_i (per unit area), strength σ_i, work of separation Γ_i, and ultimate separation Δ_U as in our previous work of enamel structures [29,30]. Many studies have shown that the cohesive law parameters have little effect on the calculation results provided that the ratio $k_i\Gamma_i/\sigma_i^2$ is sufficiently large relative to the mesh size l_e [35,36], therefore we set $k_i\Gamma_i/\sigma_i^2 l_e \approx 10$ in all calculations. Note that this assumption places a restriction on the minimum interface ductility (Δ_R/Δ_Y > 10) [37,38] for the interface model to be valid. The maximum displacement ever reached by the interface over the history of the simulation is defined as Δ_{max}, as shown in Fig. 1. This interface representation serves as a basic mixed-mode damage model with a circular failure surface. When the total displacement jump in multi-axial separation $\sqrt{\Delta_n^2+\Delta_t^2}$ (where Δ_n is the normal separation and Δ_t is the tangential separation, Fig. 1f) across an interface exceeds the larger of Δ_{max} or Δ_Y, the interface stiffness per unit area is updated to represent permanent energy dissipation, and the interface unloads along a new slope defined by Δ_{max}/σ_i. Using these cohesive parameters, the interface law was then converted to a multi-axial force–displacement relationship by scaling the interface stiffness k_i (N/m^3) and strength σ_i (N/m^2) by the interface area A_i. This scaling implies that the interface tractions are constant along the faces of the fibers, which is only valid in the limit that the relative fiber-to-interface stiffness mismatch $E_f/k_iw = (E_f/E_i)(t_i/w)$ is sufficiently large ($E_f/k_iw \approx$ 5-10 [38,39]), where t_i is the interface thickness, E_i is the interface modulus, and k_iw is the Reuss modulus of a single ply. Combined with the requirement for high fiber volume fraction ϕ_f this implies very high modulus mismatches are required ($\phi_f \sim w/t_i$) which presents another DEM model limitation.

3. "Thick" models: in-plane and transverse cracking directions

A large volume of the idealized fibrous microstructure was generated and clipped into a virtual fracture specimen ($L_m \times L_m \times L_m$ with $L_m = 50w$) with an initial crack (length $a_0 = L_m/2$) shown in Fig. 2a,e. We considered two cracking directions (Fig. 2a,e): The "transverse cracking" direction is relevant to cases of moderate damage, where the crack progresses through the thickness of the laminated panel, as could occur from flexural loading in a fish scale or an insect cuticle. The "in-plane cracking" direction corresponds to more severe cases where cracks already present through the thickness of the panel propagate in the plane of the panel, which could occur from flexural stresses or from puncture by a large wedge-like object.

To achieve stable and quasi-static crack propagation, a symmetric gradient of displacement was applied as shown on Fig. 2a,e, with the magnitude of the displacement increased slowly to propagate the crack [29,33,37,40]. This loading scenario corresponds to a mode I loading state which is typically the most dangerous in structures with pre-existing cracks [41];

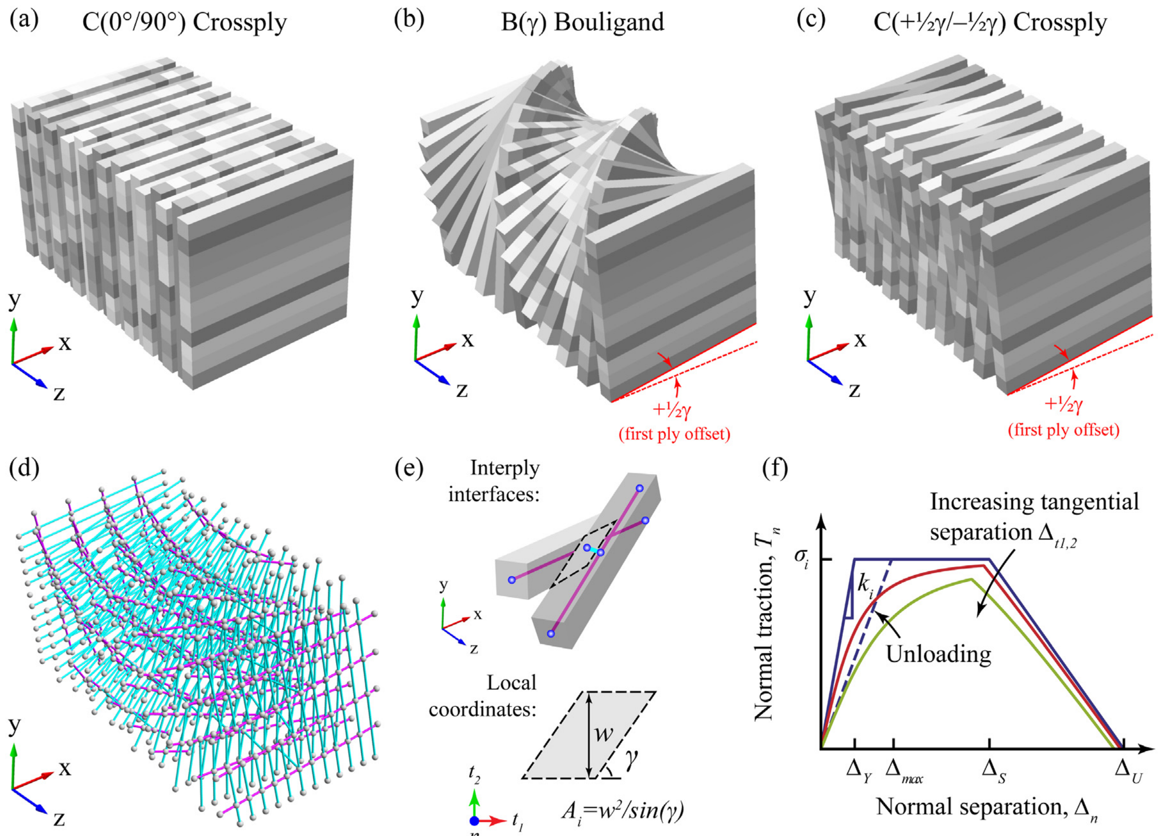

Fig. 1. Overview of the discrete element model (DEM) of the fibrous laminate structures. (a–c): Idealized composite geometry and ply stacking for the different architectures; (d) Example of full DEM mesh showing beam elements (purple) and interface elements (blue); (e) interface area definition used to compute the cohesive force and (f) Cohesive law.. (For interpretation of the references to color in this figure legend, the reader is referred to the web version of this article.)

moreover the mode I loading configuration is consistent with previous studies on Bouligand type structures [23,25,27]. The full governing dynamic equations were solved using explicit time stepping via the Newmark-β method with β = 0 [42] and with a small amount of mass and stiffness damping to eliminate high frequency dynamic effects [30]. The code was implemented in C++ and we verified the results were quasi-static by running cases with 1/2x slower loading.

Fig. 2 shows crack propagation patterns for the C(0°/90°), B(30°) and C(+15°/-15°) architectures in the transverse (Fig. 2b) and in-plane (Fig. 2f) cracking directions, obtained for fixed stiffness contrast E_f/k_iw = 5 and fixed strength contrast of σ_f/σ_i = 7.1. We note that the strength contrast was defined as the ratio of the fiber strength σ_f relative to the single-ply transverse strength σ_i. The maximum strength contrast explored in this section (σ_f/σ_i =7.1) was kept on the lower end of what would be expected in hard & soft printed polymers [43] due to computational limitations posed by edge effects; larger strength contrasts are explored in the next section. Both in-plane and transverse cracking of the C(0°/90°) crossply consisted of crack deflection at the interfaces accompanied by stress pile-up at the fibers directly ahead of the crack (Fig. 2b), which eventually fractured and restarted the deflection onto the next interface, ultimately forming a volumetric process zone. The emergent crack path consisted of broken interfaces in the first layer and broken fibers in the next layer and was on average straight. Both in-plane and transverse cracking in the B(30°) Bouligand displayed a periodic corkscrew fracture mechanism similar to experiments [18]. This mechanism was prominent when the cracks intersected plies at low angle with the crack front. In contrast, when the cracks encountered plies at high angle with the initial crack line the driving force became very small [44] and fiber fracture became prominent. In-plane failure in the C(+15°/-15°) crossply (Fig. 2b) consisted of failure mechanisms similar to those reported in our previous simulations of enamel crossplies [29] as well as experiments [31]: The crack tended to deflect along interfaces forming a kink-branch path followed by periodic pinning of the branch. In this mechanism, the interface crack would get pinned at the fiber crossing points causing fiber stress to increase; ultimately the fibers would break and the process would repeat itself with a spatial period aligned with the periodic microstructure. As the pinning was more prolonged at the fiber junctions, greater spreading of the inelastic region and enhanced energy dissipation occurred. Transverse failure of the C(+15°/-15°) crossply was similar except the kink-branch formed and grew perpendicular to the main crack. Fig. 2c,g shows the non-dimensional load–deflection curves for the in-plane and transverse cracking directions corresponding to the three architectures for σ_f/σ_i = 7.1. In all cases the curves showed an initial linear elastic region until a peak force was reached, corresponding to the onset of crack propagation. After that point the load decreased progressively as the crack propagated, except for the C(0°/90°) in the transverse cracking direction for which the load was sustained. The work of fracture (WOF) was computed as the area under the non-dimensional force–displacement curves up to the peak load and is indicated on Fig. 2c,g under each curve. The B(30°) and C(+15°/-15°) displayed comparable WOF for a given loading orientation and both were consistently higher in the transverse direction; the C(0°/90°) crossply showed the highest energy absorption which was also in the transverse direction.

For each case we also computed the 3D J-integral [45], which we used to determine the initiation toughness R_{init} for both cracking directions and as function of ply angle and strength

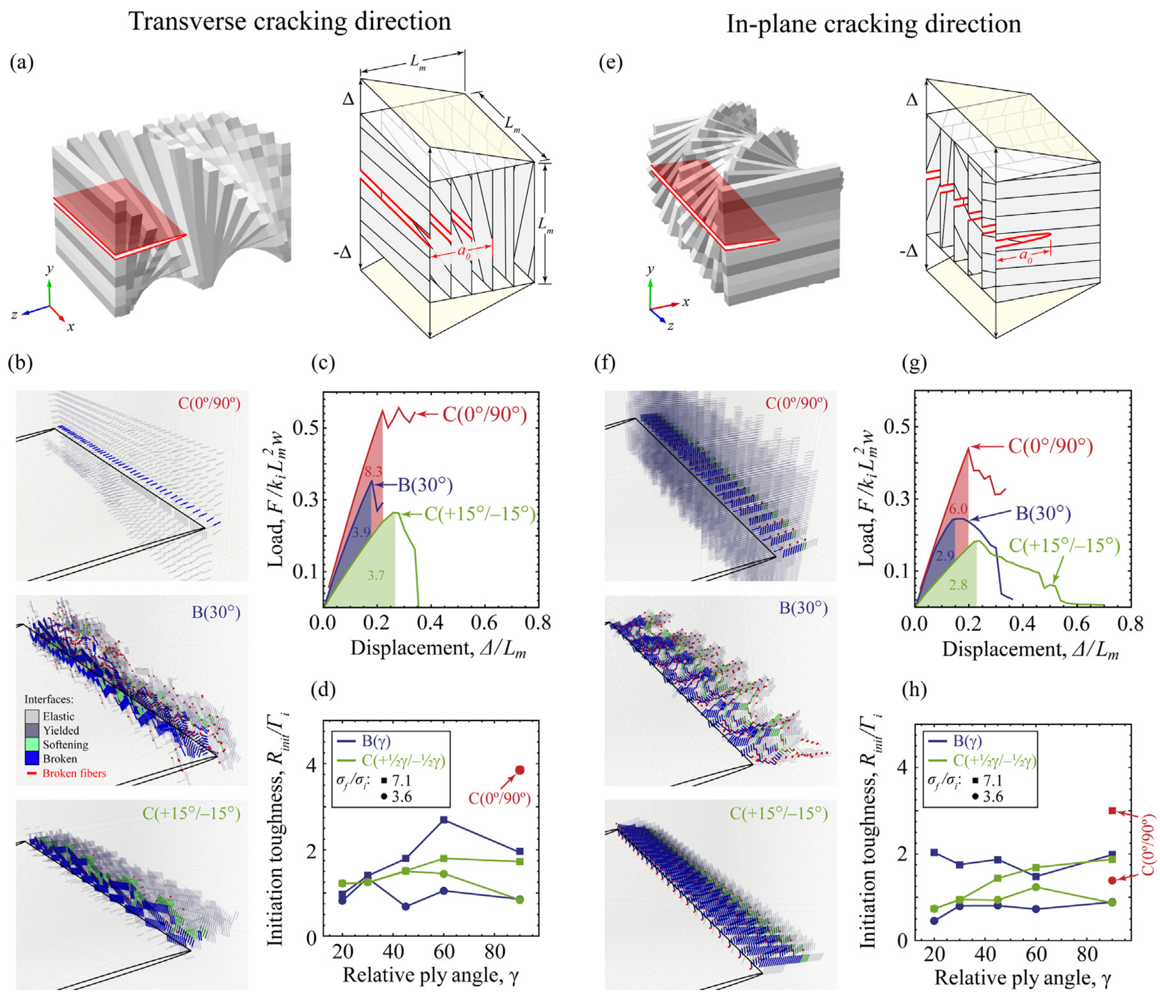

Fig. 2. Results for crack models in the transverse and in-plane cracking directions. (a,e): Model setup and crack orientations; (b,f): Snapshots of crack propagation for the different architectures showing elastically deformed interfaces, yielded interfaces, softened interfaces, broken interface as well as broken fibers; (c,g): Example of force–displacement responses for the different architectures, also showing values for work of fracture (areas under curved up to peak); (d,h): Initiation toughness as computed from 3D J-integrals as function of relative ply angle γ for the different architectures, and for two contrasts of strength σ_f/σ_i = 3.6 and 7.1. Stiffness contrast is fixed to $E_f/kiw = 5$.

contrast (Fig. 2d,h). The J-integral is a fracture mechanics based criterion and in the limit that the specimen is much larger than the nonlinear damage region, it represents the crack resistance as a true material property that is independent of specimen size, shape, and loading configuration [41,44]. We verified that this limit was achieved for most cases by running 2x larger specimens (L_m*=2L_m) and comparing the results. Thus, the results for crack resistance and toughness shown subsequently are material properties and apply to any loading scenario, including far field loading or direct loading on the crack faces (e.g., 'biting' load). For low strength contrast (i.e. relatively weak fibers) the effect of architecture on R_{init} was minimal because the fracture of individual fibers was prominent and little crack deflection was observed. As the strength contrast was increased the type of architecture and the ply angle had a much more pronounced effect on crack propagation and toughness, with the C(0°/90°) crossply emerging as the toughest architecture across all ply angles by a factor of ∼2-4x. The initiation toughness for the C(0°/90°) crossply was unaffected by strength contrast (indicated by overlapping data points in Fig. 2d) because for this architecture crack initiation was governed by the fracture of the interfaces.

4. "Thin" models with periodicity, in-plane direction

In this section we considered models that are semi-infinite and periodic in the out-of-plane *(z)* direction (Fig. 1). This allowed for larger in-plane dimensions ($L_m \times L_m \times \infty$ with L_m=150w) to be modeled because the out-of-plane dimensions only consisted of a single period of the microstructure. These models could capture large process zones and enabled higher strength contrasts (up to σ_f/σ_i = 14.3) at a reasonable computational cost, however these models were specialized to in-plane crack propagation. In the semi-infinite models, full periodicity could be represented with just three plies in the crossply models, and 180° /γ (integer) plies in the Bouligand models. Periodic boundary conditions were enforced by inserting tie constraints between nodes in the first and last ply. Due to periodicity of the microarchitecture and loading in the z-direction (Fig. 1), the emergent crack pattern was also assumed periodic for the in-plane direction (this was confirmed in Section 3, e.g. Fig. 2). Fig. 3 shows the effect of ply angle for B(γ) Bouligand and C($+\frac{1}{2}\gamma/-\frac{1}{2}\gamma$) crossply for fixed strength contrast σ_f/σ_i= 10.7 and fixed stiffness contrast $E_f/ki\,w$ = 5 (for reference the C(0°/90°) is also shown).

We observed crack deflection, delamination, fiber fracture and process zone, the extent of these mechanisms being strong functions of the type of architecture and of ply angle. The Bouligand

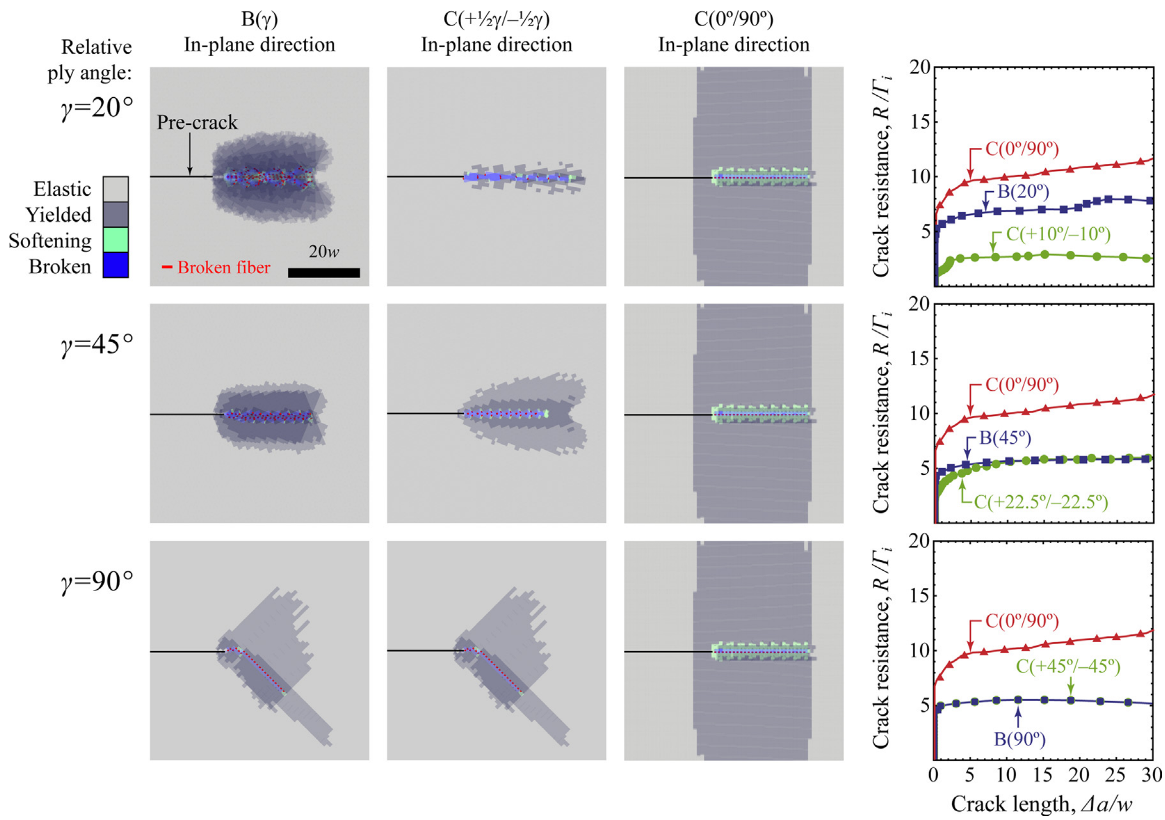

Fig. 3. Snapshots of models taken at a crack propagation $\Delta a/w \approx 30$ for three types of architectures and at three different ply angles γ. The snapshots show the damage zones and reflect the amount of energy dissipated locally around the crack. The fiber strength contrast was fixed at $\sigma_f/\sigma_i = 10.7$. The corresponding crack propagation curves (obtained from 3D J-integrals) are also shown. Snapshots are shown clipped at 1/3 of the total specimen size.

showed a larger process zone for smaller ply angle, while the C($+\frac{1}{2}\gamma/-\frac{1}{2}\gamma$) showed a larger process zone for large ply angle. In both the B(γ) Bouligand and C($+\frac{1}{2}\gamma/-\frac{1}{2}\gamma$) crossply, the process zone became asymmetric for γ= 90°. In all cases, the amount of crack deflection (indicated by softening of the cohesive law) and process zone size was much larger in the C(0°/90°) crossply. All models showed a rising crack resistance curve indicative of progressive toughening mechanisms. Interestingly the crack resistance of the Bouligand architecture decreased with increasing γ while the C($+\frac{1}{2}\gamma/-\frac{1}{2}\gamma$) crossply toughness increased, but for all angles both composites were outperformed by the C(0°/90°) crossply. The C($+\frac{1}{2}\gamma/-\frac{1}{2}\gamma$) crossply consistently shows the lowest crack resistance. Fig. 4 shows the effect of relative fiber strength for a fixed relative ply angle. For all models, stronger fibers delayed fiber fracture, increased the amount of crack deflection and caused the process zone to spread over larger volumes, in a way consistent with our previous simulations on tooth enamel [29,30]. The Bouligand structure developed delamination patterns along a periodic twisted-corkscrew, creating a "flower-like" process zone. In each ply the inelastic region is skewed along the fibers in that ply, a phenomenon which is similar to plastic zone ahead of a crack in an anisotropic elastic–plastic materials [46]. Interestingly, this presents an advantage for the Bouligand structure: the flower process zone (also observed in the phase field models in [19]) spreads more uniformly in all directions which tends to keep the damage localized, as opposed to the C(0°/90°) crossply where the damage zone is highly eccentric and can reach specimen boundaries faster. In both the C($+\frac{1}{2}\gamma/-\frac{1}{2}\gamma$) crossply and the C(0°/90°) crossply the respective mechanisms were similar as described in the models above (Fig. 3). The crack resistance curves show that increasing relative fiber strength increased overall toughness and toughening as crack propagated (higher slope or "tear modulus" on the crack resistance curve); this trend is expected and again consistent with our previous DEM models of enamel [29,30]. The C(0°/90°) crossply outperformed the other architectures in terms of initiation toughness, propagation toughness and tear modulus except for the case of low fiber strength (σ_f/σ_i= 7.1) and a γ = 30°, which was the only case where the toughness of the Bouligand was the highest.

Fig. 5a,b summarizes the effect of ply angle and relative fiber strength on initiation and average crack resistance (average of fracture toughness over a crack propagation distance of 10w). For the lowest strength contrast (i.e. low relative fiber strength) fiber fracture was prominent, there was less crack deflection and the crack "ignored" the architecture. As a result, the B(γ) Bouligand, C($+\frac{1}{2}\gamma/-\frac{1}{2}\gamma$) crossply, and C(0°/90°) crossply had comparable crack resistance (R∼2-5Γ_i). Increasing the strength contrast increased crack deflection, the size of the process zone and the fracture toughness. In general fracture toughness increased for higher ply angles. Interestingly, the Bouligand structures showed no substantial increase in average crack resistance for γ > 20-30° (Fig. 5b). The C(0°/90°) crossply consistently outperformed both B(γ) Bouligand and C($+\frac{1}{2}\gamma/-\frac{1}{2}\gamma$) crossplies and in terms initiation toughness (∼1.2-10x greater) and average crack resistance (∼5-10x greater). When comparing the respective performance of Bouligand with other types of crossply laminates, mechanical isotropy must be taken into account. Fig. 5c shows the modulus as a function of loading angle θ derived using a simple elasticity model [25] with $E_f/ki\ w$ = 5 and γ = 30° for the Bouligand architecture. As expected the C(0°/90°) crossply is more anisotropic in-plane compared to the Bouligand structure. C(0°/90°) is the stiffest laminate, but only when pulled along or near the direction of the fibers (θ =0° or θ =b90°). When pulled at 45° from the fibers (θ =b45°), the C(0°/90°) laminate is much softer: three

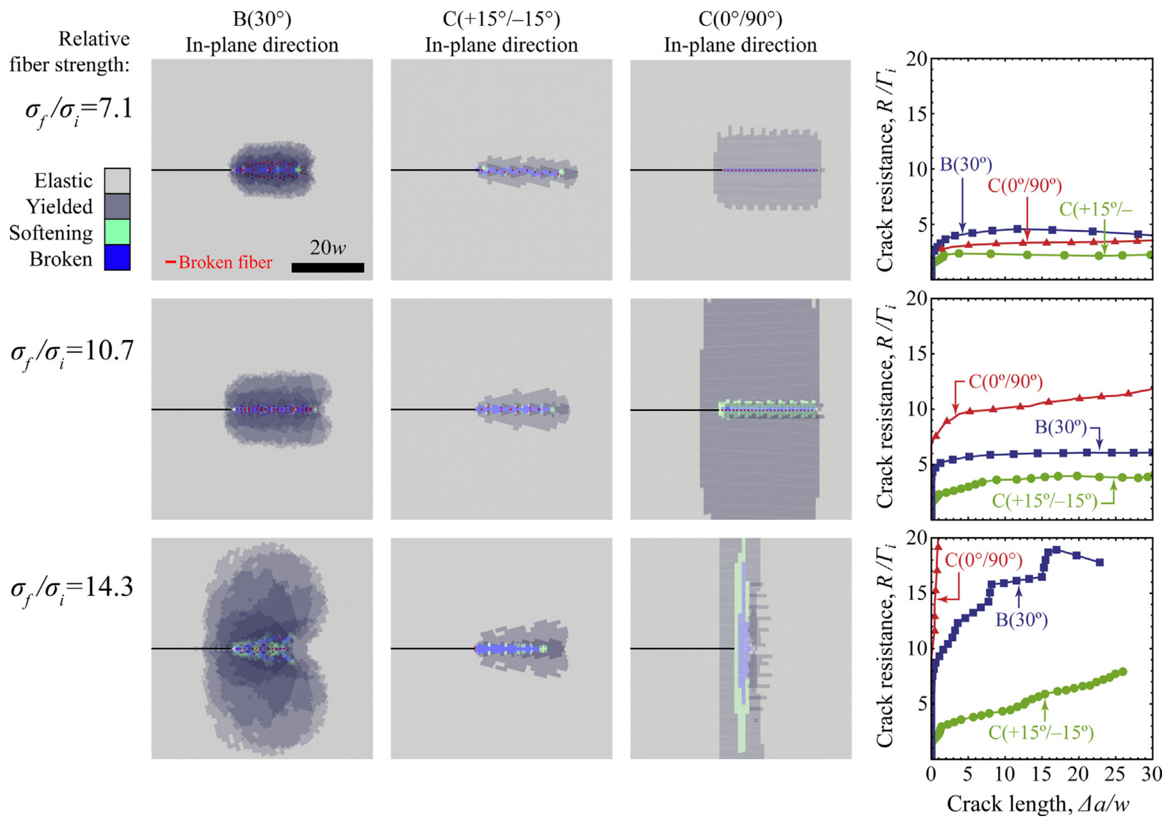

Fig. 4. Snapshots of models taken at a crack propagation $\Delta a/w \approx 30$ for three types of architectures and at three different strength contrasts σ_f/σ_i. The ply angles was fixed at $\gamma = 30°$. The fiber strength contrast was fixed at $\sigma_f/\sigma_i = 10.7$. The corresponding crack propagation curves (obtained from 3D J-integrals) are also shown. Snapshots are shown clipped at 1/3 of the total specimen size. Note that in the last curve for $\sigma_f/\sigma_i = 14.3$, we have only shown limited data prior to the process zone reaching the specimen boundaries; after this point the *R*-curve data is no longer valid due to size effects.

times less stiff than along the fibers and about half the stiffness of the Bouligand. This result is well known in laminates: a larger distribution of ply angles across the thickness of the laminate tends to average out extreme values, and produces more isotropic responses [47]. Interestingly the in-plane fracture toughness for these materials, computed using the DEM models presented here, follows a different scenario. Fig. 5d shows the initiation and propagation toughness for the Bouligand structure (γ=30°, interpolated across θ), which is near isotropic in plane for low ply angles. The fracture toughness for the C(0°/90°) crossply is the highest when the crack propagates at 0° or 90° from the fibers, because half of the fibers act as obstacles at 90° from the crack line, which is the orientation that produces the strongest crack pinning. In that configuration the C(0°/90°) is significantly tougher than the Bouligand, in terms of both initiation and propagation toughness. Propagating a crack at 45° from the fibers in the C(0°/90°) crossply produces less toughness because the efficacy of the fibers as obstacles and as bridging elements are reduced. A surprising result is that in this weakest cracking direction, the toughness of the C(0°/90°) is still higher or near equal to the Bouligand toughness. This illustrates that the combined effect of the offset asymmetric process zone and partial fiber bridging in the C(0°/90°) case offset at 45° is still act in more powerful ways than the flower-like process zone in the Bouligand B(30°).

Therefore the C(0°/90°) is more anisotropic than the Bouligand, but it is also tougher in any in-plane direction. This result is in contrast with modulus, where very high stiffness in some directions imply that the laminate is much softer in other directions. Fracture toughness is indeed not simply about averaging different directions and homogenization, as is done to predict in plane modulus. The interaction between a crack and fibers involve local mechanisms (crack pinning, deflection, bridging) which produce more complex dependence on crack orientation. In this case, the DEM models show that the in-plane toughness of C(0°/90) is higher than the Bouligand for any in-plane direction.

5. Discussion and conclusions

Crack propagation and fracture toughness in fibrous laminates involves crack deflection, twisting, delamination, bridging, process zone and fiber fracture, which can be extremely expensive or even prohibitive to capture computationally. Here we show that the discrete element method can capture these mechanisms at a fraction of computational cost of other numerical methods. Here we use these capabilities to run a large number of fracture models that aim to compare different types of 3D fibrous cross plies. The main conclusions are summarized as follows:

- Our DEM simulations captured the main failure mechanisms observed in experiments and other simulations for different types of lamellar composites. Corkscrew type fracture with periodic fiber fracture was observed in the Bouligand models [18]. Crack deflection, alternating kink-branching, and periodic pinning was observed in the C($+\frac{1}{2}\gamma/-\frac{1}{2}\gamma$) crossply models [29,31]. Interface deflection, direct fiber fracture, and periodic pinning were the main mechanisms observed in the C(0°/90°) crossply models.
- When relatively weak fibers are considered, the fracture of individual fibers is the prevailing failure mode and the crack "ignores" the fibrous architecture. Overall fracture toughness was similar in the C($+\frac{1}{2}\gamma/-\frac{1}{2}\gamma$) crossply, C(0°/90°) crossply , and B(γ) Bouligand models for weak fibers. While not considered here, we hypothesize that introducing ductility into the fibers (e.g., using a strain-controlled failure

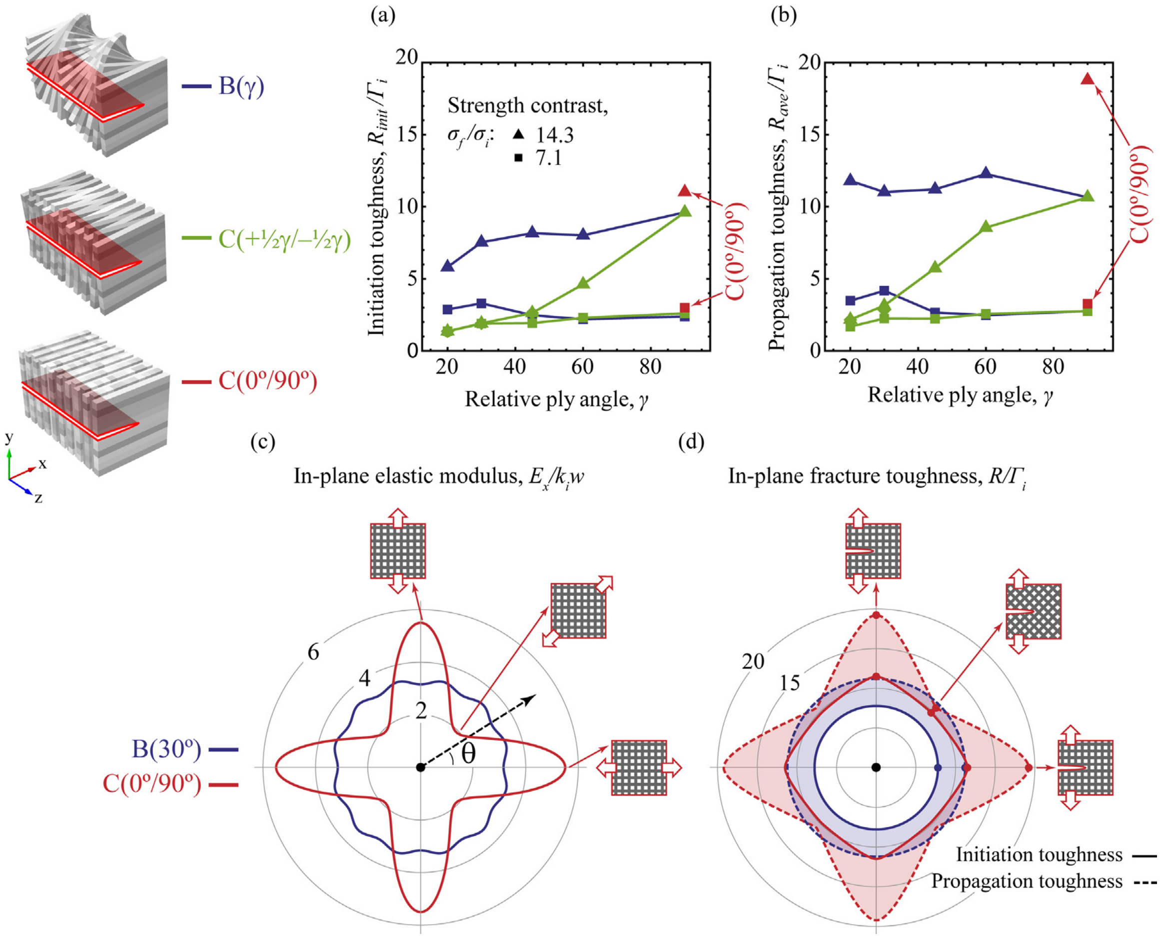

Fig. 5. Overview of in-plane properties for the three different architectures: (a) initiation toughness and (b) average crack resistance as a function of relative ply angle γ and strength contrast σ_f/σ_i for the B(γ) Bouligand, C($+\frac{1}{2}\gamma/-\frac{1}{2}\gamma$) crossply, and C(0°/90°) crossply. The average crack resistance was taken over the range $0<\Delta a<10w$. (c) In-plane modulus and (d) In-plane toughness (initiation and propagation) as function of loading direction θ for the B(30°) Bouligand and the C(0°/90°) crossply for $\sigma_f/\sigma_i = 14.3$.

criterion) would enhance the toughness through fiber bridging.

- When higher fiber strength was considered, many architecture-dependent fracture mechanisms were observed. Crack twisting was captured in the Bouligand structure, but this particular toughening mechanisms was not as effective as crack pinning by fibers positioned as obstacles directly ahead of the crack, which in turn spread a process zone over larger volume and amplifying crack resistance or energy absorption. These mechanisms were prominent in crossply designs with strong fibers.
- The Bouligand structures obtained a small but consistent relative maximum in toughness for $\gamma \approx$ 20-30°.
- Our DEM simulations predict that the C(0°/90°) crossply laminate is the toughest of all designs, for all cracking orientations (through cracks, in-plane cracks with various orientations). As opposed to Bouligand, the toughness of the C(0°/90°) shows a strong anisotropy in-plane, but surprisingly toughness is consistently higher than Bouligand for any cracking orientation.

More refinements may be brought to our DEM models in the future, including more detailed postprocessing of the interface strain state (parsing of shear/normal components) and better geometric representation of the fibers and interfaces. In particular waviness could be implemented into the fiber geometry, which has been observed in some hard biocomposites such as enamel and captured in biological growth models [13,48]; It is hypothesized that waviness would reduce deformation in the off-axis plies (e.g., the C(0°/90°) crossply) and provide a bridging mechanism that could increase toughness. Additionally, the DEM models could be improved by considering fibers with more complex (non-square) cross-sections; this would require calibration with partial 3D FEA models and combining them into the DEM formulation (e.g., similar to Dugue et al. [49]), as the fiber 'interfaces' are 3D and nonplanar. In future DEM models we could also relax the assumption of the existence of an initial pre-crack. This would allow us to capture crack nucleation events due to highly localized sharp biting (arthropod cuticle) or far-field cyclic wear and tear (plants, wood, bone) and offer a more complete comparison of evolutionary features. In general other types of DEM-based virtual experiments could be considered for more detailed comparisons such as Mode II/III cracking, dynamic impact loading, open-hole tests, and fatigue. The models presented here only capture trends in crack resistance and are not necessarily expected to carry over to other properties such as ballistic impact resistance, where studies have shown that the 0°/90° crossply and Bouligand structures perform similarly [50]. Overall, however, we believe that the DEM models as presented here capture the main fracture mechanisms for natural fibrous crossplies and enable the prediction of fracture toughness to a level of accuracy that allows comparison between different designs. The main result is that the C(0°/90°) crossply, present in plants, woods, bone or fish scales, outperforms the Bouligand structure found in arthropod cuticle and some fish scales. Despite this result, the Bouligand structure has persisted across billions of year of evolution, which suggests that features other than toughness make this particular architecture functionally attractive: in plane isotropy that could be beneficial for multiaxial loading, damage zone confinement, or perhaps advantages in growth efficiency or repair.

Declaration of competing interest

The authors declare that they have no known competing financial interests or personal relationships that could have appeared to influence the work reported in this paper.

Acknowledgments

This research was funded by a Discovery Grant from the Natural Sciences and Engineering Research Council of Canada. Computations were performed on the supercomputers Graham and Cedar at University of Waterloo and Simon Fraser University respectively, managed by Compute Canada. The operation of these supercomputers is funded by the Canada Foundation for Innovation (CFI).

Appendix. Glossary of symbols

a_0	Initial crack length
A_i	Interface area at fiber intersections
B(γ)	Bouligand structure
C($+\frac{1}{2}\gamma/-\frac{1}{2}\gamma$)	Crossply structure
C($0^o/90^o$)	Standard $0^o/90^o$crossply structure
E_f	Fiber modulus
E_i	Interface modulus
E_x	In-plane elastic modulus
F	Total specimen reaction force
k_i	Interface stiffness
l_e	Fiber element length & mesh size
L_m	Fracture specimen model size
R	Crack resistance of fracture model
R_{ave}	Average propagation toughness
R_{init}	Initiation toughness
t_i	Interface thickness
w	Fiber cross section width & height
Δa	Instantaneous crack length
Δ	Applied displacement magnitude
Δ_{max}	Interface maximum displacement
Δ_n	interface normal displacement
Δ_S	Interface softening displacement
Δ_t	Interface tangential displacement
Δ_U	Interface ultimate displacement
Δ_Y	Interface yielding displacement
Γ_i	Interface work of separation
ϕ_f	Fiber volume fraction
γ	Relative ply angle
ρ_f	Fiber mass density
σ_f	Fiber strength
σ_i	Interface strength

References

[1] S.A. Wainwright, W.D. Biggs, J.D. Currey, J.M. Gosline, Mechanical Design in Organisms, Princeton University Press, 1976.
[2] H. Peterlik, P. Roschger, K. Klaushofer, P. Fratzl, From brittle to ductile fracture of bone, Nature Mater. 5 (1) (2006) 52–55.
[3] A. Khayer Dastjerdi, F. Barthelat, Teleost fish scales amongst the toughest collagenous materials, J. Mech. Behav. Biomed. Mater. 52 (2015) 95–107.
[4] M.F. Ashby, K.E. Easterling, R. Harrysson, S.K. Maiti, The fracture and toughness of woods, Proc. R. Soc. Lond. Ser. A Math. Phys. Eng. Sci. 398 (1815) (1985) 261–280.
[5] E.A. Zimmermann, B. Gludovatz, E. Schaible, N.K. Dave, W. Yang, M.A. Meyers, R.O. Ritchie, Mechanical adaptability of the Bouligand-type structure in natural dermal armour, Nat. Commun. 4 (2013).
[6] I. Burgert, P. Fratzl, Plants control the properties and actuation of their organs through the orientation of cellulose fibrils in their cell walls, Integr. Comp. Biol. 49 (1) (2009) 69–79.
[7] S. Weiner, H.D. Wagner, The material bone: Structure mechanical function relations, Annu. Rev. Mater. Sci. 28 (1998) 271–298.
[8] S. Kamat, X. Su, R. Ballarini, A.H. Heuer, Structural basis for the fracture toughness of the shell of the conch Strombus gigas, Nature 405 (6790) (2000) 1036–1040.
[9] D. Zhu, C.F. Ortega, R. Motamedi, L. Szewciw, F. Vernerey, F. Barthelat, Structure and mechanical performance of a ‘‘modern’’ fish scale, Adv. Energy Mater. 14 (4) (2012) B185–B194.
[10] L. Kuhn-Spearing, H. Kessler, E. Chateau, R. Ballarini, A. Heuer, S. Spearing, Fracture mechanisms of the strombus gigas conch shell: implications for the design of brittle laminates, J. Mater. Sci. 31 (24) (1996) 6583–6594.
[11] D. Zhu, C.F. Ortega, R. Motamedi, L. Szewciw, F. Vernerey, F. Barthelat, Structure and mechanical performance of a modern fish scale, Adv. Energy Mater. 14 (4) (2012) B185–B194.
[12] W. Yang, V.R. Sherman, B. Gludovatz, M. Mackey, E.A. Zimmermann, E.H. Chang, E. Schaible, Z. Qin, M.J. Buehler, R.O. Ritchie, Protective role of Arapaima gigas fish scales: structure and mechanical behavior, Acta Biomater. 10 (8) (2014) 3599–3614.
[13] B.N. Cox, How the tooth got its stripes: patterning via strain-cued motility, J. R. Soc. Interface 10 (84) (2013) 20130266.
[14] J.F.V. Vincent, U.G.K. Wegst, Design and mechanical properties of insect cuticle, Arthropod Struct. Dev. 33 (3) (2004) 187–199.
[15] D. Raabe, C. Sachs, P. Romano, The crustacean exoskeleton as an example of a structurally and mechanically graded biological nanocomposite material, Acta Mater. 53 (15) (2005) 4281–4292.
[16] S. Ifuku, M. Nogi, K. Abe, M. Yoshioka, M. Morimoto, H. Saimoto, H. Yano, Preparation of chitin nanofibers with a uniform width as α-chitin from crab shells, Biomacromolecules 10 (6) (2009) 1584–1588.
[17] R. Yang, A. Zaheri, W. Gao, C. Hayashi, H.D. Espinosa, AFM Identification of beetle exocuticle: Bouligand structure and nanofiber anisotropic elastic properties, Adv. Funct. Mater. 27 (6) (2017) 1603993.
[18] J.C. Weaver, G.W. Milliron, A. Miserez, K. Evans-Lutterodt, S. Herrera, I. Gallana, W.J. Mershon, B. Swanson, P. Zavattieri, E. DiMasi, The stomatopod dactyl club: a formidable damage-tolerant biological hammer, Science 336 (6086) (2012) 1275–1280.
[19] S. Yin, W. Yang, J. Kwon, A. Wat, M.A. Meyers, R.O. Ritchie, Hyperelastic phase-field fracture mechanics modeling of the toughening induced by Bouligand structures in natural materials, J. Mech. Phys. Solids 131 (2019) 204–220.
[20] E.A. Zimmermann, B. Gludovatz, E. Schaible, N.K. Dave, W. Yang, M.A. Meyers, R.O. Ritchie, Mechanical adaptability of the Bouligand-type structure in natural dermal armour, Nat. Commun. 4 (2013) 2634.
[21] S. Murcia, E. Lavoie, T. Linley, A. Devaraj, E.A. Ossa, D. Arola, The natural armors of fish: a comparison of the lamination pattern and structure of scales, J. Mech. Behav. Biomed. Mater. 73 (2017) 17–27.
[22] W. Huang, D. Restrepo, J.Y. Jung, F.Y. Su, Z. Liu, R.O. Ritchie, J. McKittrick, P. Zavattieri, D. Kisailus, Multiscale toughening mechanisms in biological materials and bioinspired designs, Adv. Mater. 31 (43) (2019) 1901561.
[23] N. Suksangpanya, N.A. Yaraghi, R.B. Pipes, D. Kisailus, P. Zavattieri, Crack twisting and toughening strategies in Bouligand architectures, Int. J. Solids Struct. 150 (2018) 83–106.
[24] M. Moini, J. Olek, J.P. Youngblood, B. Magee, P.D. Zavattieri, Additive manufacturing and performance of architectured cement-based materials, Adv. Mater. 30 (43) (2018) 1802123.
[25] A. Zaheri, J.S. Fenner, B.P. Russell, D. Restrepo, M. Daly, D. Wang, C. Hayashi, M.A. Meyers, P.D. Zavattieri, H.D. Espinosa, Revealing the mechanics of helicoidal composites through additive manufacturing and beetle developmental stage analysis, Adv. Funct. Mater. 28 (33) (2018) 1803073.
[26] Z. Yin, A. Dastjerdi, F. Barthelat, Tough and deformable glasses with bioinspired cross-ply architectures, Acta Biomater. (2018).
[27] N. Suksangpanya, N.A. Yaraghi, D. Kisailus, P. Zavattieri, Twisting cracks in Bouligand structures, J. Mech. Behav. Biomed. Mater. 76 (2017) 38–57.
[28] Z. Song, Y. Ni, S. Cai, Fracture modes and hybrid toughening mechanisms in oscillated/twisted plywood structure, Acta Biomater. 91 (2019) 284–293.
[29] J.W. Pro, F. Barthelat, Discrete element models of tooth enamel, a complex three-dimensional biological composite, Acta Biomater. 94 (2019) 536–552.
[30] J.W. Pro, F. Barthelat, Discrete element models of fracture in tooth enamel: Failure mode competition and statistical effects, J. Mech. Phys. Solids (2020) 103868.

[31] D. Bajaj, D.D. Arola, On the R-curve behavior of human tooth enamel, Biomaterials 30 (23–24) (2009) 4037–4046.
[32] S. Park, J. Quinn, E. Romberg, D. Arola, On the brittleness of enamel and selected dental materials, Dent. Mater. 24 (11) (2008) 1477–1485.
[33] J.W. Pro, R.K. Lim, L.R. Petzold, M. Utz, M.R. Begley, The impact of stochastic microstructures on the macroscopic fracture properties of brick and mortar composites, Extrem. Mech. Lett. 5 (2015) 1–9.
[34] N. Abid, J.W. Pro, F. Barthelat, Fracture mechanics of nacre-like materials using discrete-element models: Effects of microstructure, interfaces and randomness, J. Mech. Phys. Solids 124 (2019) 350–365.
[35] J.W. Pro, S. Sehr, R.K. Lim, L.R. Petzold, M.R. Begley, Conditions controlling kink crack nucleation out of, and delamination along, a mixed-mode interface crack, J. Mech. Phys. Solids 121 (2018) 480–495.
[36] J. Parmigiani, M. Thouless, The roles of toughness and cohesive strength on crack deflection at interfaces, J. Mech. Phys. Solids 54 (2) (2006) 266–287.
[37] J.W. Pro, R.K. Lim, L.R. Petzold, M. Utz, M.R. Begley, GPU-based simulations of fracture in idealized brick and mortar composites, J. Mech. Phys. Solids 80 (2015) 68–85.
[38] M.R. Begley, N.R. Philips, B.G. Compton, D.V. Wilbrink, R.O. Ritchie, M. Utz, Micromechanical models to guide the development of synthetic 'brick and mortar' composites, J. Mech. Phys. Solids 60 (8) (2012) 1545–1560.
[39] N. Abid, M. Mirkhalaf, F. Barthelat, Discrete-element modeling of nacre-like materials: Effects of random microstructures on strain localization and mechanical performance, J. Mech. Phys. Solids 112 (2018) 385–402.
[40] N. Abid, J.W. Pro, F. Barthelat, Fracture mechanics of nacre-like materials using discrete-element models: Effects of microstructure, interfaces and randomness, J. Mech. Phys. Solids (2018).
[41] T.L. Anderson, Fracture Mechanics: Fundamentals and Applications, CRC Press, 2017.
[42] X.-P. Xu, A. Needleman, Numerical simulations of fast crack growth in brittle solids, J. Mech. Phys. Solids 42 (9) (1994) 1397–1434.
[43] M.F. Ashby, D. Cebon, Materials selection in mechanical design, Le J. Phys. IV 3 (C7) (1993) C7–1–C7–9.
[44] H. Tada, P.C. Paris, G.R. Irwin, The Stress Analysis of Cracks, Handbook, Del Research Corporation, 1973.
[45] M. Chiarelli, A. Frediani, A computation of the three-dimensional J-integral for elastic materials with a view to applications in fracture mechanics, Eng. Fract. Mech. 44 (5) (1993) 763–788.
[46] G. Xin, W. Hangong, K. Xingwu, J. Liangzhou, Analytic solutions to crack tip plastic zone under various loading conditions, Eur. J. Mech. A Solids 29 (4) (2010) 738–745.
[47] R.F. Gibson, Principles of Composite Material Mechanics, CRC Press, 2016.
[48] B. Cox, A. multi scale, Discrete-cell simulation of organogenesis: Application to the effects of strain stimulus on collective cell behavior during ameloblast migration, J. Theoret. Biol. 262 (1) (2010) 58–72.
[49] M. Dugue, M. Fivel, Y. Bréchet, R. Dendievel, Indentation of interlocked assemblies: 3D discrete simulations and experiments, Comput. Mater. Sci. 79 (2013) 591–598.
[50] L. Vargas-Gonzalez, S.M. Walsh, J. Wolbert, Impact and Ballistic Response of Hybridized Thermoplastic Laminates, Army Research Lab Aberdeen Proving Ground Md Weapons and Materials Research …, 2011.